Angewandte Chemie International Edition

Angewandte International Edition Chemie

How to cite: *Angew. Chem. Int. Ed.* **2026**, e6865093
doi.org/10.1002/anie.6865093

RESEARCH ARTICLE

Covalently Hydrophobic Nanocarbon Supported Ni Single-Atom Catalysts for Highly Selective CO_2 Electroreduction

Yanzheng Ji[1,2] | Huaizhu Wang[3] | Yuxiao Meng[4] | Chongyi Ling[4] | Zhikang Cheng[1] | Chunhui Liu[1] | Xinquan Yu[1] | Zuoxiu Tie[3] | Yan Xiong[3] | Jinlan Wang[4] | Zhong Jin[3] | Youfa Zhang[1]

[1]Jiangsu Key Laboratory of Advanced Metallic Materials, School of Materials Science and Engineering, Southeast University, Nanjing, Jiangsu, China | [2]School of Chemical Engineering, Yangzhou Polytechnic Institute, Yangzhou, Jiangsu, China | [3]State Key Laboratory of Coordination Chemistry, MOE Key Laboratory of Mesoscopic Chemistry, MOE Key Laboratory of High Performance Polymer Materials and Technology, Jiangsu Key Laboratory of Green Energy Catalysis and Intelligent Chemical Engineering, Suzhou Key Laboratory of Green Intelligent Manufacturing of New Energy Materials and Devices, Tianchang New Materials and Energy Technologies Research Center, Institute of Green Chemistry and Engineering, School of Chemistry and Chemical Engineering, Nanjing University, Nanjing, Jiangsu, China | [4]Key Laboratory of Quantum Materials and Devices of Ministry of Education, School of Physics, Southeast University, Nanjing, Jiangsu, China

Correspondence: Jinlan Wang (jlwang@seu.edu.cn) | Zhong Jin (zhongjin@nju.edu.cn) | Youfa Zhang (yfzhang@seu.edu.cn)

Received: 11 February 2026 | **Revised:** 23 April 2026 | **Accepted:** 13 May 2026

Keywords: CO_2 reduction reaction | hollow carbon spheres | hydrophobic | microenvironment | Ni single-atom catalyst

ABSTRACT

Precise tailoring of hydrophobic microenvironments surrounding catalytic active sites has emerged as a critical strategy for enhancing the efficiency of electrochemical CO_2 reduction reaction. However, covalent modulation of catalyst hydrophobicity is rarely reported, and the mechanistic influence of hydrophobicity-driven interfacial catalysis remains unclear. Herein, we report a general synthetic methodology for the covalent immobilization of structurally tunable hydrophobic alkyl chains onto nanocarbon-loaded single-atom catalysts. The covalently hydrophobic nanocarbon supported Ni single-atom catalysts deliver near-unity CO selectivity over a broad potential range from −0.5 to −1.2 V (versus the reversible hydrogen electrode) in flow cells. Integrated spectroscopic, computational kinetic, and thermodynamic analyses reveal that the alkyl chains form hydrophobic barriers by disrupting interfacial water networks, resulting in a 0.37 eV increase in energy barrier of the hydrogen evolution reaction. The hydrophobic micro-environment further stabilizes the *COOH intermediate under aqueous conditions, lowering its formation Gibbs energy (ΔG) by 0.17 eV relative to unmodified catalysts. This work establishes a universal hydrophobic modification strategy for carbon-based catalysts that breaks the conventional activity-selectivity trade-off in aqueous electrocatalysis, opening new opportunities for optimizing gas-consumption electrochemical reactions.

1 | Introduction

Electrochemical conversion of CO_2 into value-added fuels and chemicals using renewable electricity offers a sustainable route for carbon recycling and climate change mitigation [1]. However, the sluggish CO_2 diffusion in aqueous electrolytes and the competing hydrogen evolution reaction (HER) limit the activity and selectivity of electrochemical CO_2 reduction reaction (CO_2RR), hindering its large-scale applications [2]. In addition to catalyst design, rational control of the electrochemical microenvironment (e.g., local pH, solvation effects, ion concentration gradients, and hydrophobicity) significantly enhances CO_2RR activity and

Yanzheng Ji, Huaizhu Wang and Yuxiao Meng contributed equally to this work.

selectivity [3–7]. Interfacial hydrophobicity has been shown to strongly influence reaction kinetics, product selectivity, and conversion efficiency in gas-involving electrochemical reactions [8–11]. It is well-known that the CO_2RR and HER are competing reactions, both of which are thermodynamically feasible in the operating potential range of the CO_2RR, and the HER reactants (H_2O or H^+) are typically abundant near the electrode [12]. The catalyst's hydrophobic microenvironment can restrict the supply of proton donors (H_2O) at the electrode-electrolyte interface, suppressing the competing HER [13]. Furthermore, the catalyst's hydrophobicity can enhance the local gas environment, increasing the contact area between the catalyst and CO_2 gas [14]. This facilitates CO_2 enrichment near the catalyst, reducing mass transfer limitations, and thus improving efficiency and selectivity [15, 16].

So far, a handful of strategies have been explored to regulate the hydrophobic characteristics of catalytic microenvironments, most of which rely on physical methods to construct extrinsic hydrophobicity. Common approaches include mixing or coating the catalysts with hydrophobic materials such as hydrophobic graphite [9], per-fluorinated polymers [13, 16, 17], or alkanethiols [11, 18]. These studies have clearly demonstrated the significant impacts of the local gas/liquid environments on the catalysts in gas-involving electrochemical reactions. However, physical modification strategies face significant limitations: (1) Surface coatings may block active sites; (2) Hydrophobic polymers may increase interfacial resistance and energy consumption; (3) Physically adhered layers are prone to detachment under operating conditions [3, 19]. Because these methods depend on non-covalent interactions, they inherently suffer from poor long-term stability and durability. Consequently, the development of covalent hydrophobic modification strategies—capable of permanently integrating hydrophobic functionality into the catalyst structure—is both urgent and essential. In recent years, nitrogen (N)-doped carbon-loaded single-atom catalysts (SACs) have emerged as promising materials for catalyzing the electrochemical reduction of CO_2 to C_1 products, owing to their unique electronic properties and high atom utilization efficiency [2, 20, 21]. N doping serves as a crucial strategy in the CO_2RR by modulating the electronic structure of catalysts, enhancing CO_2 adsorption, and facilitating the formation of critical intermediates [22]. Among various N-doped carbon architectures, hollow carbon nanospheres stand out as three-dimensional supports with abundant exposed active sites and efficient mass transport pathways [23, 24]. The N-doped carbon nanospheres, serving as the host for the metal SACs, play a crucial role in determining the wettability of the catalysts. However, during the high-temperature pyrolysis treatment, the micro-crystallites within the nanocarbon materials exhibit limited long-range order and possess abundant edge/defect sites. The dangling bonds at these sites react with moisture to form oxygen-containing functional groups, imparting the inherent hydrophilicity of the carbon support [25]. Furthermore, nanocarbon materials often exhibit high chemical stability due to their paucity of active functional groups [26]. Hence, it remains a significant challenge to establish covalently hydrophobic properties on nanocarbon support.

In this study, we develop a class of CO_2RR catalysts by synthesizing N-doped hollow carbon nanospheres (NCNS) hosting atomically dispersed Ni-N_4 sites via a hard-template method. Furthermore, the hydrophobicity of these catalysts is precisely tuned by covalently grafting alkyl chains of varying lengths onto the carbon nanosphere support (termed as Ni-N_4/C_n-NCNS, where n = 2, 3, or 6). The optimized Ni-N_4/C_2-NCNS catalyst compared to an initial Ni-N_4/NCNS catalyst shows substantially decreased HER activity and higher Faradaic efficiency for CO production (FE_{CO}), and outstanding waterflooding-resistant ability. The enhanced catalytic performance originates from an optimized gas/liquid/solid interfacial microenvironment, which synergistically reduces interfacial water layer density while increasing the energy barrier of the HER, thermodynamically stabilizes the *COOH intermediate by lowering its formation ΔG, and promotes efficient CO_2 mass transport and utilization through physical confinement and chemical adsorption.

2 | Results and Discussion

The specific preparation steps of hydrophobic Ni-N_4/C_n-NCNS catalysts are schematically illustrated in Figure 1. Firstly, monodisperse, mesoporous melamine-formaldehyde (MF) polymer nanospheres are synthesized via an aqueous emulsion polymerization self-assembly strategy, serving as hard templates (Figures S1, S2) [27]. Subsequently, the MF nanospheres are added into a Tris-HCl buffer containing dopamine to form a polydopamine (PDA) shell [28]. The abundant phenolic hydroxyl and amino groups on the PDA layer facilitate the coordination and chelation of Ni^{2+} cations, forming MF@PDA-Ni (Figures S3–S5) [29, 30]. Moreover, this method provides a versatile platform, enabling the facile substitution of the Ni^{2+} with various metal cations, such as Fe^{3+}, Co^{2+}, Cu^{2+}, Sn^{4+}, etc [31–34]. The MF component of MF@PDA-Ni, with a reported decomposition temperature of 550°C [35], underwent partial degradation and shrinkage during pyrolysis at 900°C under N_2. The PDA shell, however, remained intact, leading to the formation of hollow Ni-N_4/NCNS catalyst (Figure S6). Finally, alkyl chlorosilanes react with surface hydroxyl groups of the Ni-N_4/NCNS catalyst via a nucleophilic substitution under mild conditions, covalently grafting alkyl chains onto the catalyst surface, yielding the hydrophobic Ni-N_4/C_n-NCNS catalyst.

The thermal decomposition of MF introduces N atoms into the PDA shell, increasing the N content in Ni-N_4/NCNS (8.45 at%), predominantly as pyridinic N (Figure S7, S8). Raman spectra (I_D/I_G = 3.99) confirm a high defect density in the carbon framework (Figure S9). Nitrogen adsorption-desorption measurements show that Ni-N_4/NCNS displayed a high Brunauer-Emmett-Teller (BET) surface area of 850 $m^2\ g^{-1}$ with hierarchical porosity spanning micropores, mesopores, and macropores (Table S1 and Figure S10). Aberration-corrected high-angle annular dark field scanning transmission electron microscopy (HAADF-STEM) confirmed the uniform dispersion of Ni single atoms (~0.2 nm) across the carbon framework (Figure 2a). This uniformity of Ni atom distribution is attributed to the negatively charged, ligand-rich MF@PDA precursor, which provides abundant anchoring sites for stable Ni atom immobilization (Figure S11). Inductively coupled plasma optical emission spectroscopy (ICP-OES) analysis has been carried out to quantify the Ni content (0.84 wt%).

Transmission electron microscopy (TEM) image analysis revealed Ni-N_4/C_n-NCNS as uniform, monodisperse particles (~150 nm; Figure 2b). Moreover, corresponding energy-dispersive

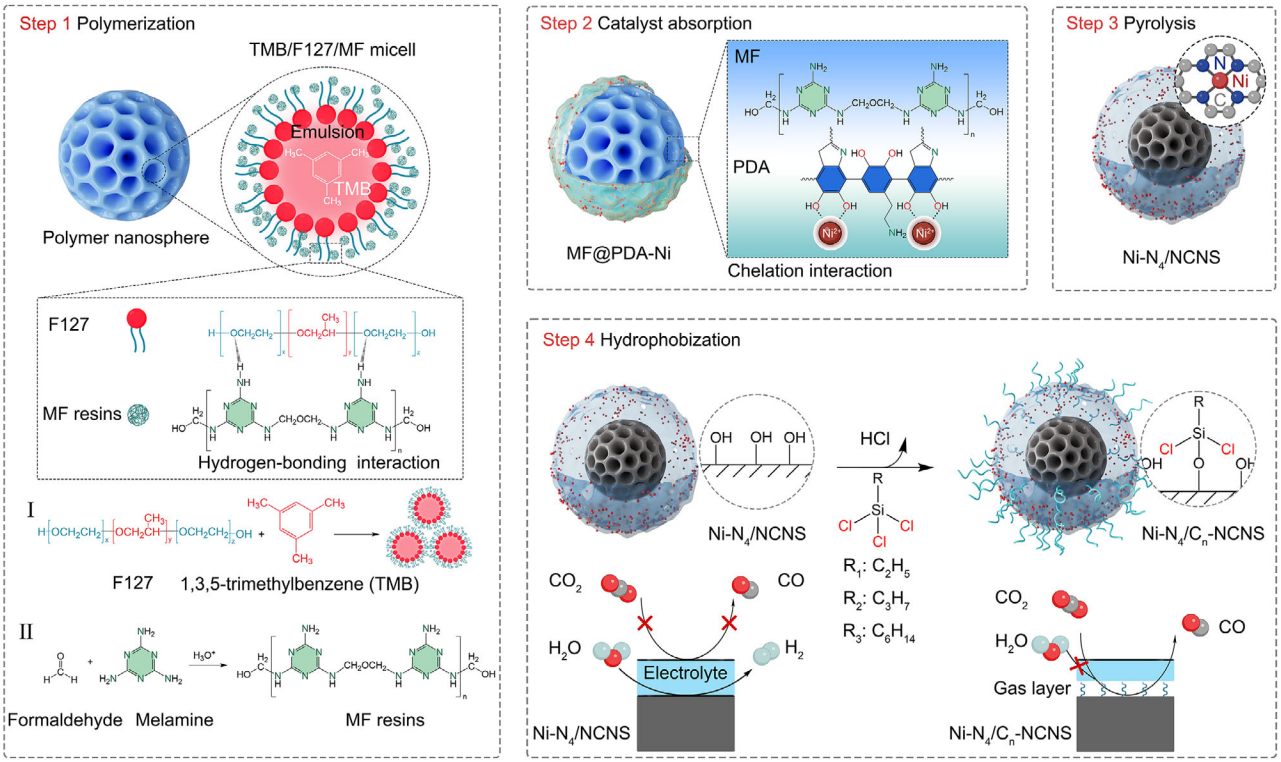

FIGURE 1 | Schematic illustration of the catalyst preparation. The Ni-N_4/NCNS and Ni-N_4/C_n-NCNS catalysts are prepared via a four-step process: (1) polymerization to prepare MF nanospheres, (2) polydopamine coating with Ni^{2+} absorption, (3) pyrolysis to generate Ni single-atom sites, and (4) hydrophobization with chlorosilane for stable gas film formation.

X-ray spectroscopy (EDS) elemental mapping revealed a homogeneous distribution of Ni, N, O, Si, Cl and C elements, with no observable Ni aggregation (Figure 2c, Figure S12). The Fourier transform infrared (FTIR) spectrum of Ni-N_4/C_2-NCNS exhibited new absorption bands corresponding to the stretching vibrations of -CH_3 (2961 cm^{-1}) and -CH_2- (2881 cm^{-1}) groups, as well as a Si-O stretching vibration at 1108 cm^{-1}, confirming the successful covalent grafting of alkyl chains onto the Ni-N_4/NCNS surface (Figure 2d). The X-ray diffraction (XRD) pattern of Ni-N_4/C_2-NCNS displayed only two broad peaks (26.2° (002), 44.0° (004)) attributed to graphitic carbon, with no diffraction signals corresponding to metallic Ni (PDF#04-0850), indicating the absence of crystalline Ni phases (Figure 2e).

The elemental and electronic status of Ni-N_4/C_2-NCNS were probed using X-ray photoelectron spectroscopy (XPS) and X-ray absorption fine structure (XAFS) analyses. High-resolution N 1s XPS spectra revealed the coexistence of various N configurations, including pyridinic N (398.2 eV), coordinated Ni-N (399.4 eV), pyrrolic N (400.5 eV), graphitic N (401.2 eV), and oxidized N (403.1 eV) (Figure S8) [2]. The observed Ni $2p_{3/2}$ peak at 854.9 eV indicated a mixed valence state for Ni, lying between metallic (Ni^0, 853.5 eV) and divalent states (Ni^{2+}, 855.8 eV) (Figure 2f). To elucidate the local coordination environment and the modulated electronic effects at the Ni site, we conducted XAFS spectroscopy. The Ni K-edge X-ray absorption near-edge structure (XANES) spectra of Ni-N_4/C_2-NCNS revealed an absorption edge positioned between those of metallic Ni and NiO (Figure 2g). These findings suggested that the Ni ions in Ni-N_4/C_2-NCNS exhibited an intermediate oxidation state between metallic Ni^0 and Ni^{2+}. A dominant peak at 1.38 Å, characteristic of Ni-N coordination, was observed in both the wavelet transform (Figure S13) and Fourier transform (Figure 2h) analyses of the X-ray absorption fine structure spectrometry (EXAFS) spectra for Ni-N_4/C_2-NCNS. In contrast, the Ni foil exhibited a typical Ni-Ni peak at 2.20 Å, while the Ni-O interaction in NiO appeared at ~1.62 Å. Quantitative EXAFS fitting demonstrated that the Ni atoms in Ni-N_4/C_2-NCNS were four-fold coordinated by N atoms, forming a square planar geometry (Figure 2i, Figure S14, Table S2).

We evaluated the underwater adhesion behaviors of CO_2 bubbles and the air-phase surface wettability of Ni-N_4/C_n-NCNS and Ni-N_4/NCNS catalysts. The Ni-N_4/NCNS catalyst exhibited an underwater contact angle (UCA) for CO_2 bubbles of approximately 152° (Figure 3a). In contrast, the Ni-N_4/C_n-NCNS catalyst showed remarkably lower UCA values (16-67°) for CO_2 bubbles, demonstrating exceptional surface aerophilicity (Figure 3b, Figure S15). Underwater CO_2 adhesion measurements revealed that Ni-N_4/C_2-NCNS achieved an adhesion force of 291.8 μN, more than double that of unmodified Ni-N_4/NCNS (134.7 μN, Figure 3c). The high N-doping level endowed the Ni-N_4/C_2-NCNS with a remarkable CO_2 adsorption capacity of 2.69 mmol g^{-1} (Figure 3d) [36]. In air, Ni-N_4/NCNS exhibited a water contact angle (WCA) of approximately 45.9°, indicating its hydrophilic surface properties (Figure 3e). The WCA of Ni-N_4/C_2-NCNS exhibited a significant increase, reaching 115.0°, with hydrophobicity increasing progressively with alkyl chain length, reaching a maximum value of 134.7° (Figure S16). While Ni-N_4/NCNS dispersed readily in water, the hydrophobic surface of Ni-N_4/C_n-NCNS prevented water infiltration, forming a stable separate phase (Figure 3f). Upon immersion, hydrophobic surfaces tend to trap ambient gas bubbles, forming a persistent gas film [37],

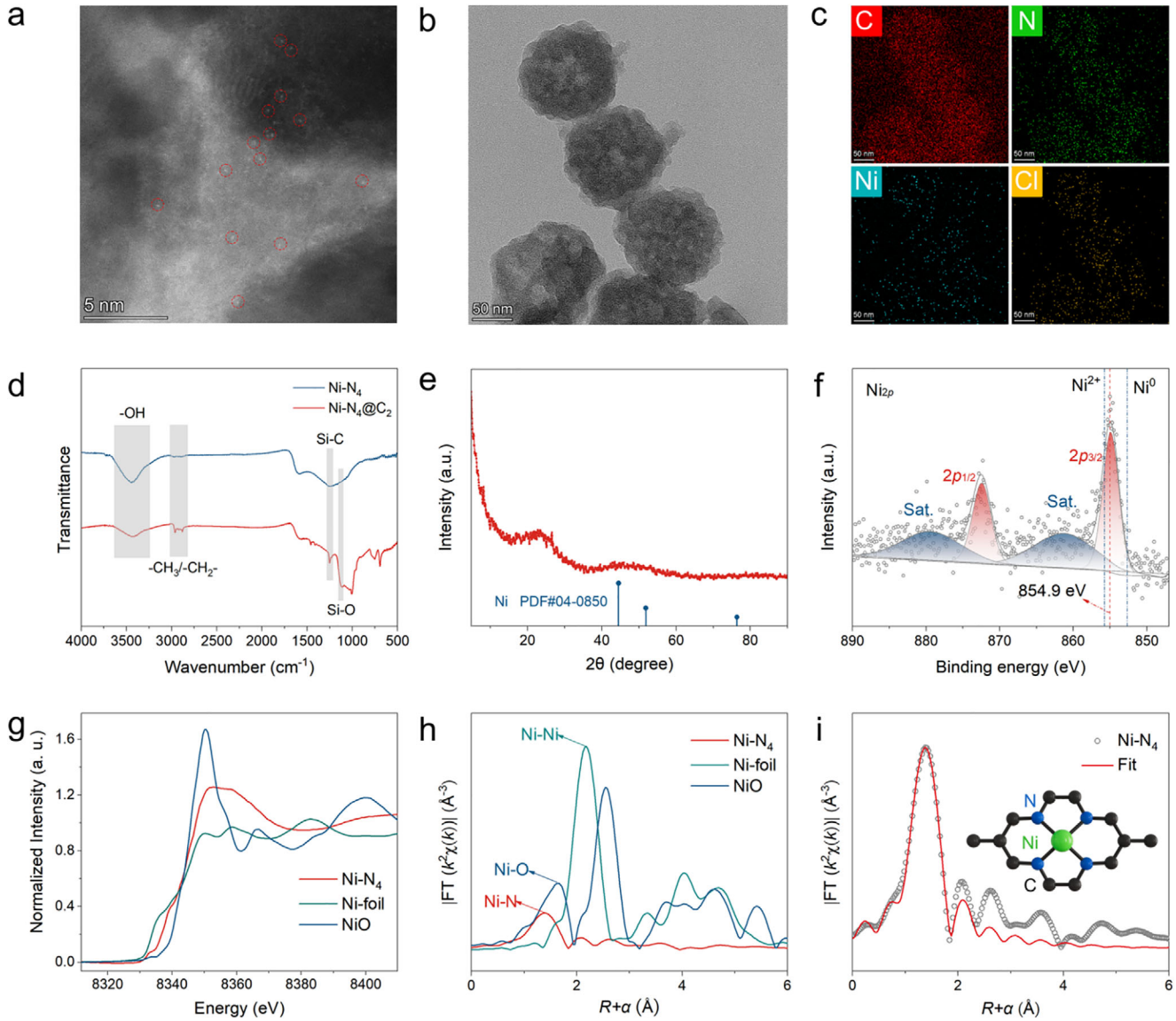

FIGURE 2 | Catalyst structural characterizations. (a) Atomic-resolution HAADF-STEM image of Ni-N_4/NCNS. (b, c) High resolution TEM image and corresponding EDS elemental mapping images for C, N, Ni, O, Si and Cl elements of Ni-N_4/C_2-NCNS. (d) The FTIR spectra of Ni-N_4/NCNS and Ni-N_4/C_2-NCNS. (e) XRD pattern of Ni-N_4/C_2-NCNS, in comparison with standard XRD of Ni metal. (f) Ni 2p XPS spectra of Ni-N_4/NCNS. (g) Ni K-edge XANES spectra of Ni-N_4/NCNS, Ni foil and NiO (R space plots). (h) Fourier transform of the EXAFS spectra at R-space of Ni-N_4/NCNS, Ni foil and NiO. (i) The fittings of the Fourier-transform (FT) EXAFS spectra of Ni-N_4 for Ni K edge. The inset shows the most likely coordination structure of Ni sites in Ni-N_4.

and the high surface roughness of the nanoparticle catalysts can further enhance the bubble adhesion [38]. The covalently hydrophobic Ni-N_4/C_2-NCNS catalyst, by virtue of its strong affinity for CO_2 bubbles, ensures a continuous CO_2 supply to the active sites and facilitates rapid diffusion of CO_2 from the exterior to the interior catalytic regions. This synergy between underwater aerophilicity and surface hydrophobicity optimizes reaction kinetics for efficient underwater CO_2 electroreduction.

The CO_2RR performances of all the synthesized catalysts were initially evaluated in a conventional H-type electrochemical cell containing 0.1 M $KHCO_3$ electrolyte saturated with CO_2. Nuclear magnetic resonance (NMR) spectroscopy and online gas chromatography were used to identify and quantify the gas and liquid products, respectively. Product analysis definitively identified CO and H_2 as the exclusive products of the reaction, with no other gaseous or liquid products detected (Figure S17). The linear sweep voltammetry (LSV) curves were employed to investigate the electrochemical performance of the catalyst (Figure S18). In the specified voltage range, higher total current densities were observed under a CO_2 atmosphere compared to an Ar atmosphere, confirming preferential CO_2 reduction over the competing HER. Among the catalysts with varying alkyl chain lengths (Ni-N_4/C_n-NCNS, $n = 2, 3, 6$), Ni-N_4/C_6-NCNS exhibited the lowest current density, indicating that excessive hydrophobicity adversely affects catalytic performance (Figure 4a). The hydrophobic alkyl chain modification reduced catalytic activity, likely due to impaired proton reduction kinetics and/or diminished electrical conductivity [5, 11]. Notably, the robust core–shell structure ensured excellent stability, demonstrating consistent

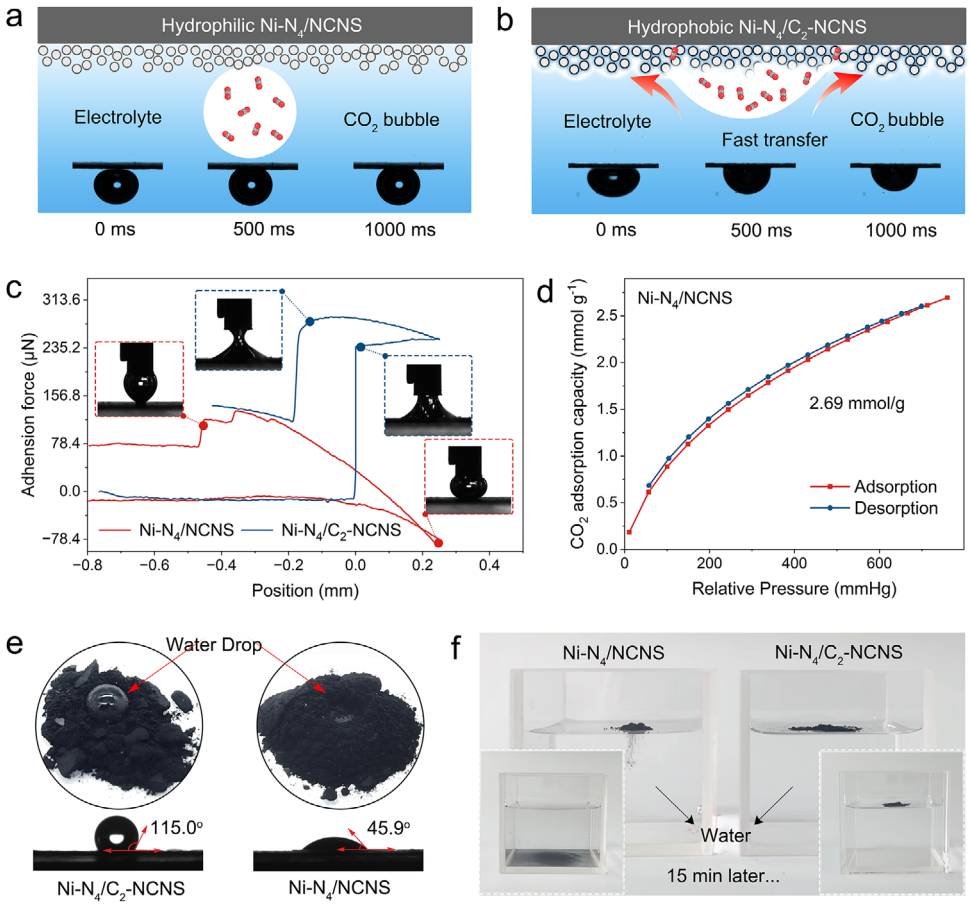

FIGURE 3 | Wettability evaluation. (a, b) Underwater CO_2-bubble adhesion behaviors and schematic illustration of Ni-N_4/NCNS and Ni-N_4/C_2-NCNS; (c) Adhesion force curve of CO_2 bubble in contacted with Ni-N_4/NCNS and Ni-N_4/C_2-NCNS, with corresponding digital photos. (d) CO_2 adsorption/desorption isotherms of Ni-N_4/NCNS; (e) Digital images of water droplets on Ni-N_4/NCNS and Ni-N_4/C_2-NCNS, with corresponding WCA; (f) Photographs of catalysts dispersion in water at the initial state and after 15 min.

current response at −0.7 to −1.1 V vs. RHE (Figure S19). Potentiostatic tests revealed the Ni-N_4/NCNS catalyst only achieved a maximum FE_{CO} of 78.0% at -0.8 V (Figure 4b). However, Ni-N_4/C_2-NCNS catalysts demonstrated exceptional FE_{CO} exceeding 74.2% over a broad potential range of −0.7 to −1.1 V versus RHE, achieving a maximum FE_{CO} of 96.6% at −0.8 V versus RHE. Interestingly, increased hydrophobicity did not universally enhance FE_{CO}. In contrast, Ni-N_4/C_n-NCNS exhibited significantly suppressed HER activity relative to Ni-N_4/NCNS over −0.8 to −1.1 V vs. RHE (Figure 4c). At −1.0 V versus RHE, Ni-N_4/NCNS yielded a FEH_2 of 38.3%, whereas Ni-N_4/C_2-NCNS reached only 2.3%. Electrochemical impedance spectroscopy (EIS) revealed that Ni-N_4/NCNS catalyst had a low resistance of 27.27 Ω.cm^2. In contrast, surface modification with alkyl chains decreased conductivity, increasing resistance up to 41.32 Ω.cm^2 with longer chains (Figure S20). The potential-dependent partial current densities of CO and H_2 were measured and plotted. Ni-N_4/NCNS and Ni-N_4/C_2-NCNS catalysts exhibited nearly identical CO partial current densities (~ -5.4 mA cm^{-2}) at −0.8 V versus RHE (Figure S21a). On the other hand, at −0.8 V versus RHE, the H_2 partial current density for the hydrophobic Ni-N_4/C_2-NCNS was only −0.086 mA cm^{-2}, substantially lower than −1.268 mA cm^{-2} observed for Ni-N_4/NCNS (Figure S21b). Increasing the applied voltage favored the HER, but Ni-N_4/C_2-NCNS maintained significant HER suppression within −0.7 to −1.1 V versus RHE, suggesting a non-linear relationship between hydrophobicity and HER inhibition. Excessively increasing hydrophobicity can lead to a Cassie state, reducing the crucial three-phase contact [39, 40]. To evaluate the intrinsic catalytic activity for CO products on all sample, we normalized the partial current densities (j_{CO}) by the electrochemically active surface area (ECSA) (Figure S22, S23). Notably, the Ni-N_4/NCNS catalyst exhibited 1.68-fold higher intrinsic CO production activity than the hydrophobic Ni-N_4/C_2-NCNS catalyst. The similar morphology, chemical and electronic structure of Ni-N_4/NCNS and Ni-N_4/C_2-NCNS catalysts suggested that the improved CO_2RR performance of Ni-N_4/C_2-NCNS was primarily attributed to its optimized hydrophobic microenvironment.

Next, we evaluated the CO_2RR performances of the Ni-N_4/C_2-NCNS catalyst in a membrane-electrode-assembly (MEA) reactor (Figure S24, S25). As shown in Figure 4d, Ni-N_4/NCNS exhibited significantly lower current densities than Ni-N_4/C_2-NCNS across a broad voltage range. Product selectivity was determined from controlled potential electrolysis measurements by calculating faradaic efficiency. Remarkably, Ni-N_4/C_2-NCNS achieved an outstanding FE_{CO} of 99.6% at −0.6 V versus RHE (Figure 4e), surpassing the performance of previously reported single- and bimetallic catalysts under comparable conditions. More importantly, high CO selectivities over 90% were maintained over a

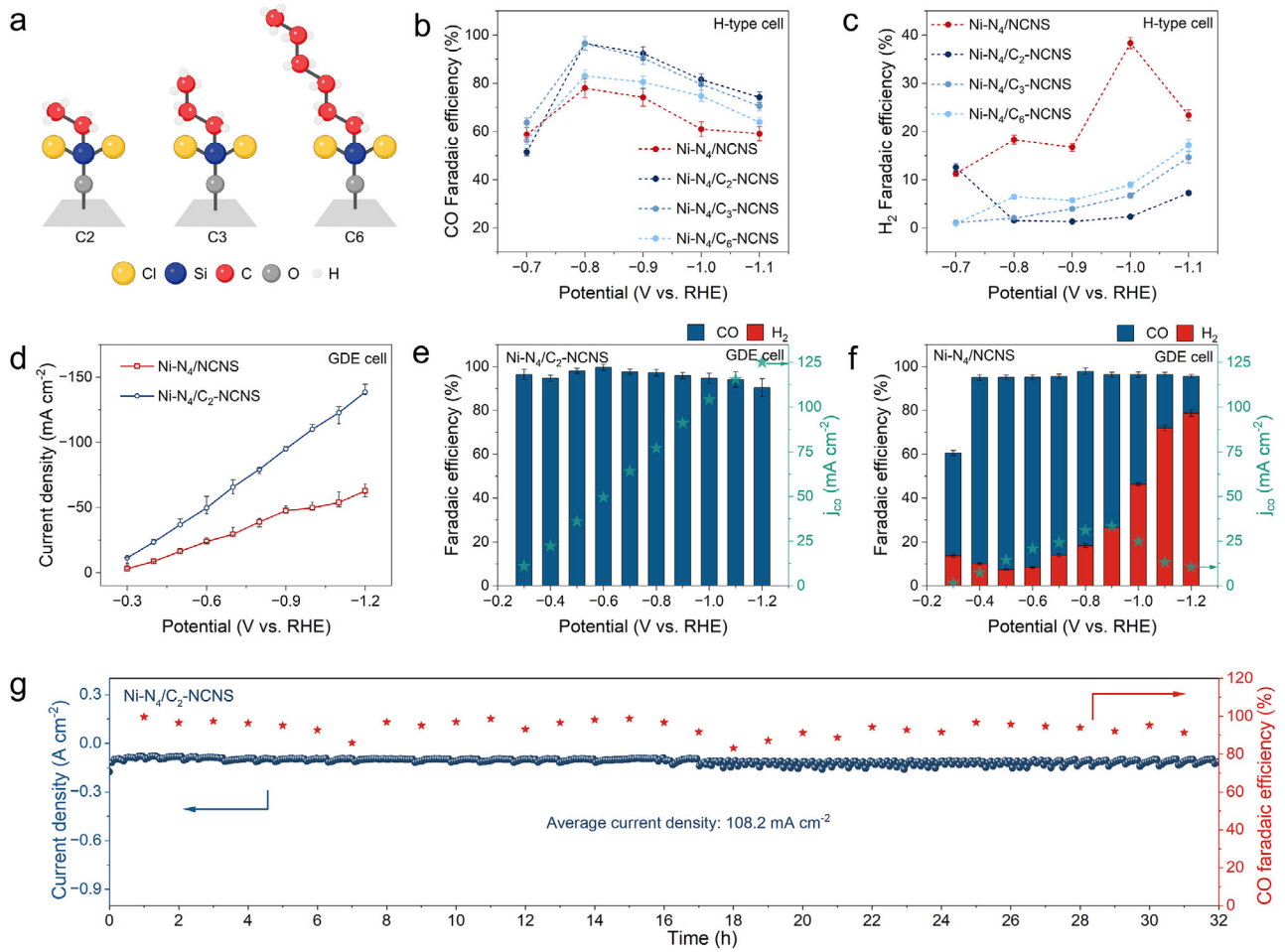

FIGURE 4 | Electrocatalytic CO2RR performance. (a) Structural schematics of the Ni-N_4/C_n-NCNS catalysts with different carbon chain lengths. (b, c) FE_{CO} and FE_{H2} at various potential versus RHE in H-type cell. (d) LSV curves of Ni-N_4/NCNS and Ni-N_4/C_2-NCNS in flow cell. (e, f) Comparison of Faradaic efficiency (left axis) and partial current density (right axis) of Ni-N_4/C_2-NCNS and Ni-N_4/NCNS catalysts at various potentials in flow cell. (g) Total current density and FE_{CO} during long-term CO_2RR stability test at around 108.2 mA cm^{-2}.

wide potential range from 0.3 to 1.2 V. At 1.1 V, Ni-N_4/C_2-NCNS showed a CO partial current density of 125.2 mA cm^{-2}, nearly 160 times higher than Ni-N_4/NCNS (Figure 4e, Figure S26). In sharp contrast, Ni-N_4/NCNS consistently demonstrated lower FE_{CO} values at all potentials. Notably, the Ni-N_4/NCNS catalyst exhibited a substantial increase in HER contribution (up to 78.7%) at high potentials, primarily due to CO_2 mass transport limitations under high current densities while proton availability remained abundant (Figure 4f). During electrolysis, the nanoscale catalyst layer can be easily flooded by the electrolyte, disrupting the three-phase interface around the active sites. In our system, the Ni-N_4/C_2-NCNS catalyst prevents complete electrolyte penetration, fostering a stable three-phase interface for efficient CO_2 electroreduction. Importantly, Ni-N_4/C_2-NCNS maintained negligible HER activity (<1%) across the entire potential range, attributable to its abundant gas-liquid-solid interfaces and hollow architecture that ensured sustained CO_2 supply during catalysis. The stability of the Ni-N_4/C_2-NCNS catalyst for CO_2RR was also evaluated in 1.0 M KOH. Ni-N_4/C_2-NCNS demonstrated excellent CO_2RR stability, maintaining consistent performance at 108.2 mA cm^{-2} with minimal potential drift and showing negligible current density loss after 32 h of operation at −0.8 V versus RHE (Figure 4g, Figure S27).

In situ Raman spectroscopy was employed to monitor the dynamic evolution of reaction intermediates on catalyst surfaces during CO_2-to-CO conversion (Figure S28). During CO_2RR from −0.2 to −1.0 V versus RHE, seven characteristic Raman bands were identified (Figures 5a, b). The bands at 418 cm^{-1} (ν_{OH}) and 480 cm^{-1} ($\delta_{H\text{-}O\text{-}H}$) correspond to O-H stretching and bending vibrations of water molecules chemisorbed on Ni single-atom sites [41]. The markedly attenuated intensity of these bands on hydrophobic Ni-N_4/C_2-NCNS indicates reduced interfacial water coverage, consistent with suppressed water aggregation induced by alkyl chain modification. The bands at 1325 cm^{-1} and 1698 cm^{-1} are assigned to the symmetric stretching of HCO_3^- ($\nu_s(CO_2^-)$) and adsorbed carbonate species (CO_3^{2-}), respectively, confirming the coexistence of electrolyte ions at the interface [42, 43]. Crucially, the formation of the key *COOH intermediate was evidenced by a set of characteristic peaks, the C-OH stretching modes at 1259 cm^{-1} and 1384 cm^{-1} [44, 45], along with the C = O stretching vibration at 1652 cm^{-1}. Their progressive intensity increase with overpotential reflects accelerated *COOH generation. This assignment is rigorously corroborated by in-situ FTIR spectra, where characteristic *COOH vibrations including $\nu_{C=O}$ (1650 cm^{-1}), $\nu_{C\text{-}OH}$ (1297 cm^{-1}), and coupled $\nu_{O\text{-}H}$ (1390 cm^{-1}) were distinctly observed (Figure S29, 30). [44, 46] Notably,

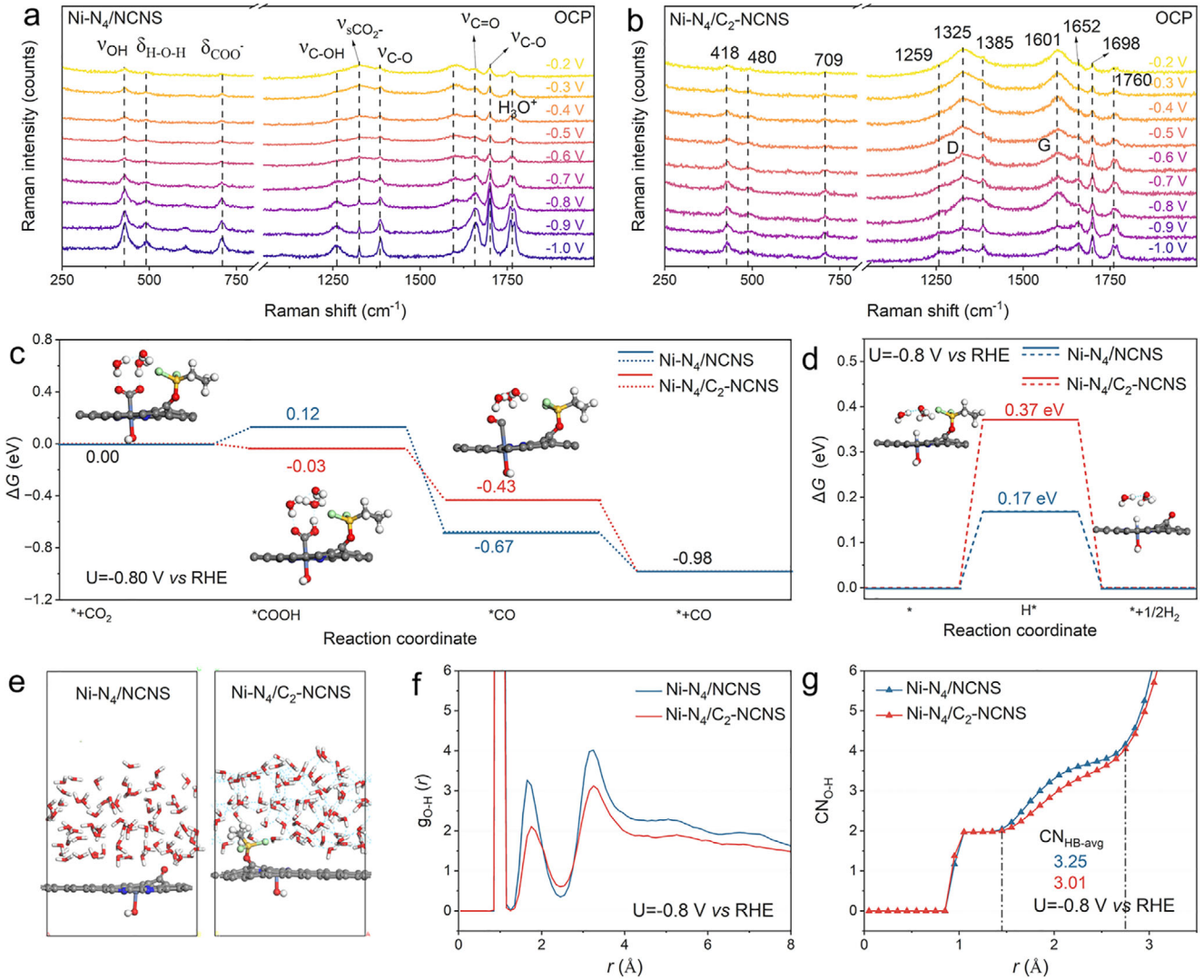

FIGURE 5 | Mechanistic investigation. (a, b) In situ Raman spectra of Ni-N_4/NCNS and Ni-N_4/C_2-NCNS. Applied potentials range from open circuit potential (OCP) to around −1.0 V vs. RHE. Gibbs energy diagrams of (c) CO_2RR and (d) HER on Ni-N_4/NCNS and Ni-N_4/C_2-NCNS at $U_{RHE} = -0.8$ V. (e) Typical models of Ni-N_4/NCNS and Ni-N_4/C_2-NCNS catalysts for AIMD simulations, featuring the catalyst surface solvated by 72 water molecules with a density of 1 g/cm^3. (f) Radial distribution functions (g(r)) of O-H hydrogen bonds surrounding the Ni centres for Ni-N_4/NCNS and Ni-N_4/C_2-NCNS catalysts. (g) Quantification of the corresponding O-H hydrogen bonds in the second coordination shell.

the detection of the $\nu_{C=O}$ band in FTIR, where the carbon G-band is inactive, unambiguously distinguishes the intermediate signal from the carbon background. The consistently weaker *COOH signals on Ni-N_4/C_2-NCNS compared with Ni-N_4/NCNS suggest faster *COOH desorption kinetics, directly correlating with the superior FECO of the hydrophobic catalyst. Meanwhile, the emerging peak at 709 cm^{-1} (OH* bend) verified the role of water as a proton donor participating in the proton-coupled electron transfer process.

To elucidate the reaction mechanism of the catalyst in the electrocatalytic CO_2RR, theoretical models of Ni–N_4/NCNS with four nitrogen atoms and an axially coordinated OH group, as well as Ni–N_4/C_2–NCNS featuring a C_2 alkyl chain coordination environment, were constructed based on insights from In-situ Raman, FTIR and XANES analyses. The In-situ Raman spectra exhibit a characteristic vibrational band at approximately 418 cm^{-1} ν(O–H) consistent with chemically adsorbed O–H species on Ni single-atom sites under reaction conditions. In addition, the FTIR spectra display new absorption bands associated with the stretching vibration of OH groups at 3445 cm^{-1}, further supporting the formation of OH species during operation. Meanwhile, the XANES analysis indicates modifications in the local coordination environment of the metal center. Accordingly, an axially coordinated OH ligand was included in the model to represent the realistic catalytic structure. Using these models, we systematically investigated the influence of the hydrophobic C_2 alkyl chain on CO_2RR activity and the competing HER under different solvation environments the effects, including an implicit solvation model, a micro-solvation model with three explicit water molecules, and a solvated model containing 72 explicit water molecules (Figure S31–S33 and Figure 5e). The explicit solvent models allow a more realistic representation of the electrochemical interface, capturing hydrogen-bond networks, proton donor/acceptor behavior, and directional interactions between solvent molecules and key intermediates. The overall

CO_2RR pathway mainly involves the activation of CO_2 at the Ni active site to form adsorbed *CO_2, followed by proton-electron coupling to generate *COOH. The adsorbed *COOH is further hydrogenated to *CO, which subsequently desorbs to produce CO. In the H-cell electrolyte (pH = 6.8), the CO formation is experimentally observed at −0.70 V with a Faradaic efficiency of 74.2%, while the maximum FE_{CO} of 96.6% at −0.8 V versus RHE. Based on this, we selected −0.80 V as a representative potential to construct the Gibbs energy diagram for CO_2 reduction to CO (Figure 5c). On the Ni–N_4/C_2–NCNS catalyst, the thermodynamic Gibbs energy along the *CO_2 − *COOH − *CO pathway exhibits a continuously downhill trend while the conversion of CO_2 to *COOH is an endergonic step, with an energy increase 0.12 eV on Ni-N_4/NCNS. This is 0.15 eV higher than that over Ni-N_4/C_2-NCNS, indicating C_2 alkyl chain modification effectively facilitating *COOH formation. For HER reaction, the adsorption *H constitutes the thermodynamic rate-determining step. Functionalization with the C_2 alkyl chain increases the *H Gibbs energy from 0.17 eV to 0.37 eV, thereby suppressing H_2 formation. In addition, ab initio molecular dynamics (AIMD) simulations were employed to assess the effect of C_2 alkyl chain modification on the reaction kinetics of HER. At the Ni active site, the electrochemical water dissociation step (Volmer step) is the key to H_2O activation, with the calculated energy barrier rising from 1.57 eV to 2.39 eV upon C_2 chain functionalization. This indicates that the introduction of C_2 alkyl chains significantly reduces the affinity for interfacial water, mainly due to its hydrophobicity, which induces a local interfacial cavity near the active site, hindering water migration and thereby making water activation and dissociation more difficult compared to clean surfaces (Figure S34, 35). Crucially, implicit solvation model, CO_2RR and HER barriers became nearly identical for both catalysts, clearly demonstrating that the alkyl chains influence catalytic performance primarily through water mediation rather than intrinsic catalyst modification (Figure S36).

To quantitatively evaluate the distribution of water around the central Ni catalyst, 10 ps AIMD simulations were performed. Analysis of the OH radial distribution function g(r) (RDFs) from the equilibrated AIMD trajectories revealed the first, second, and third solvation shell maxima at 0.95, 1.75, and 3.25 Å, respectively (Figures 5e, f). consistent with previous experimental and computational results [47], confirming that our models accurately capture the behavior of liquid water. In comparison to the Ni-N_4/NCNS system, the H densities in the second and third water solvation shells of the Ni-N_4/C_2-NCNS system were 2.11 and 3.12, respectively, both lower than those in Ni-N_4/NCNS, and the O density at 2.75 Å was also reduced, indicating that C_2 alkyl chain incorporation decreased interfacial H_2O molecule distribution. (Figure S37). To further understand the influence of the C_2 chain on water microstructure, the average hydrogen-bond coordination number (CN) around individual water molecules was extracted from the AIMD trajectories. The average CN values were 3.25 and 3.01 for Ni-N_4/NCNS and Ni-N_4/C_2-NCNS, demonstrating that alkyl chain incorporation weakened water network connectivity (Figure 5g). Overall, hydrophobic alkyl functionalization restructures the interfacial water layer, weakening water–surface interactions and disrupting the hydrogen-bond network. The resulting interfacial cavities facilitate CO_2 transport, ultimately promoting CO_2RR selectivity.

3 | Conclusion

In summary, here we report the design of a class of hollow-structured N-doped Ni single-atom catalyst, in which alkyl molecular brushes were grafted onto the catalyst surface to optimize the gas-liquid-solid microenvironments. The abundant triple-phase interfaces and hollow structure promote CO_2 enrichment near the Ni-N_4/C_2-NCNS catalyst, ensuring a sufficient supply of CO_2. The Ni-N_4/C_2-NCNS catalyst demonstrated significantly enhanced underwater aerophilicity, higher FE_{CO}, and markedly suppressed HER activity compared to Ni-N_4/NCNS catalyst. Ni-N_4/C_2-NCNS exhibits a FE_{CO} of 99.6% at 100 mA cm^{-2} under pure CO_2 feed. Through integrated electrochemical kinetics, in situ spectroscopic analysis, and computational modeling, this study elucidates the critical influence of interfacial water density modulated by hydrophobic alkyl brush on catalytic reaction mechanisms. Modulating interfacial water density suppresses proton transfer kinetics while weakening H* adsorption, thereby elevating the HER energy barrier. Moreover, it optimizes the Gibbs energy of rate-determining steps and stabilizes the COOH* intermediate, promoting efficient CO_2RR. This work presents a versatile strategy for the hydrophobic modification of nanocarbon-loaded metal atom catalysts, highlighting the significance of precisely controlling catalyst surface wettability to enhance both mass transport and reaction kinetics, with broad potential for advancing gas-involved electrocatalysis.

Author Contributions

Yanzheng Ji: conceptualization, methodology, validation, investigation, data curation, software, visualization, writing – review and editing, writing – original draft, supervision, formal analysis, project administration. **Huaizhu Wang:** methodology, data curation, validation, conceptualization, writing – original draft. **Yuxiao Meng:** software, methodology, conceptualization, validation, data curation, visualization, writing – original draft. **Chongyi Ling:** methodology, validation, software, writing – review and editing. **Zhikang Cheng:** methodology, data curation. **Chunhui Liu:** methodology, data curation. **Xinquan Yu:** supervision, resources. **Zuoxiu Tie:** writing – review and editing. **Yan Xiong:** writing – review and editing. **Jinlan Wang:** supervision, resources, project administration, formal analysis, writing – review and editing, funding acquisition. **Youfa Zhang:** methodology, supervision, resources, funding acquisition, writing – review and editing, project administration, formal analysis, visualization, conceptualization. **Zhong Jin:** conceptualization, methodology, writing – review and editing, resources, supervision, project administration, formal analysis, funding acquisition.

Acknowledgments

The work was supported by the National Key Research and Development Program of China (No. 2022YFA1503103), the National Natural Science Foundation of China (Nos. 52071076, 22479074, 22475096, 92261112, U25A20628, 22561160129), the Open Research Fund of Jiangsu Key Laboratory for Advanced Metallic Materials at Southeast University (No. AMM2021B01), the Equipment Pre-Research and Ministry of Education Joint Fund General Project (No. 8091B02052407), the Fundamental Research Program Key Project of Jiangsu Province (No. BK20253008), the Natural Science Foundation of Jiangsu Province (Nos. BK20240400, BK20241236), the Science and Technology Major Project of Jiangsu Province (No. BG2024013), the Scientific and Technological Achievements Transformation Special Fund of Jiangsu Province (No. BA2023037), the Academic Degree and Postgraduate Education Reforming Project of Jiangsu Province (No. JGKT24_C001), the Key Core Technology Open Competition Project of Suzhou City (No. SYG2024122), the Open Research

Fund of Suzhou Laboratory (No. SZLAB-1308-2024-TS005), the Gusu Leading Talent Program of Scientific and Technological Innovation and Entrepreneurship in Wujiang District of Suzhou City (No. ZXL2021273), and the Chenzhou National Sustainable Development Agenda Innovation Demonstration Zone Provincial Special Open Competition Project (Nos. 2023sfq11, 2025sfq38), and the Fundamental Research Funds for the Central Universities and Nanjing University International Collaboration Initiative (No. 020514380354).

Conflicts of Interest

The authors declare no conflict of interest.

Data Availability Statement

The data that support the findings of this study are available from the corresponding author upon reasonable request.

References

1. F. Li, A. Thevenon, A. Rosas-Hernández, et al., "Molecular Tuning of CO_2-to-Ethylene Conversion," *Nature* 577 (2020): 509–513, https://doi.org/10.1038/s41586-019-1782-2.

2. H. B. Yang, S.-F. Hung, S. Liu, et al., "Atomically Dispersed Ni(i) as the Active Site for Electrochemical CO_2 Reduction," *Nature Energy* 3 (2018): 140–147, https://doi.org/10.1038/s41560-017-0078-8.

3. R. Lu, X. Zhang, H. Shi, Z. Zhao, M. Li, and X. Zhang, "Wettability Control in Electrocatalytic CO_2 Reduction: Effects, Modulations and Mechanisms," *Applied Catalysis B: Environment and Energy* 341 (2024): 123293, https://doi.org/10.1016/j.apcatb.2023.123293.

4. J. Chen and L. Wang, "Effects of the Catalyst Dynamic Changes and Influence of the Reaction Environment on the Performance of Electrochemical CO_2 Reduction," *Advanced Materials* 34 (2022): 2103900, https://doi.org/10.1002/adma.202103900.

5. J. Lv, R. Yin, L. Zhou, et al., "Microenvironment Engineering for the Electrocatalytic CO_2 Reduction Reaction," *Angew Chem-ger Edit* 134 (2022): e202207252, https://doi.org/10.1002/ange.202207252.

6. Z.-S. Zhu, S. Zhong, C. Cheng, et al., "Microenvironment Engineering of Heterogeneous Catalysts for Liquid-Phase Environmental Catalysis," *Chemical Reviews* 124 (2024): 11348–11434, https://doi.org/10.1021/acs.chemrev.4c00276.

7. N. Govindarajan, A. Xu, and K. Chan, "How pH Affects Electrochemical Processes," *Science* 375 (2022): 379–380, https://doi.org/10.1126/science.abj2421.

8. S. Shu, T. Song, C. Wang, H. Dai, and L. Duan, "[2+1] Cycloadditions Modulate the Hydrophobicity of Ni-N_4 Single-Atom Catalysts for Efficient CO_2 Electroreduction," *Angewandte Chemie International Edition* 63 (2024): e202405650, https://doi.org/10.1002/anie.202405650.

9. C.-T. Dinh, T. Burdyny, M. G. Kibria, et al., "CO_2 Electroreduction to Ethylene via Hydroxide-Mediated Copper Catalysis at an Abrupt Interface," *Science* 360 (2018): 783–787, https://doi.org/10.1126/science.aas9100.

10. H. Li, W. Fang, L.-X. Wang, et al., "Physical Regulation of Copper Catalyst With a Hydrophobic Promoter for Enhancing CO_2 Hydrogenation to Methanol," *The Innovation* 4 (2023): 100445, https://doi.org/10.1016/j.xinn.2023.100445.

11. D. Wakerley, S. Lamaison, F. Ozanam, et al., "Bio-Inspired Hydrophobicity Promotes CO_2 Reduction on a Cu Surface," *Nature Materials* 18 (2019): 1222–1227, https://doi.org/10.1038/s41563-019-0445-x.

12. X. Sheng, W. Ge, H. Jiang, and C. Li, "Engineering the Ni–N–C Catalyst Microenvironment Enabling CO_2 Electroreduction With Nearly 100% CO Selectivity in Acid," *Advanced Materials* 34 (2022): 2201295, https://doi.org/10.1002/adma.202201295.

13. J. Chen, H. Qiu, Y. Zhao, et al., "Selective and Stable CO_2 Electroreduction at High Rates via Control of Local H_2O/CO_2 Ratio," *Nature Communications* 15 (2024): 5893, https://doi.org/10.1038/s41467-024-50269-1.

14. J. Fu, H. Zhang, H. Du, et al., "Unveiling the Interfacial Species Synergy in Promoting CO_2 Tandem Electrocatalysis in Near-Neutral Electrolyte," *Journal of the American Chemical Society* 146 (2024): 23625–23632, https://doi.org/10.1021/jacs.4c08844.

15. M. Fang, M. Wang, Z. Wang, et al., "Hydrophobic, Ultrastable $Cu^{\delta+}$ for Robust CO_2 Electroreduction to C_2 Products at Ampere-Current Levels," *Journal of the American Chemical Society* 145 (2023): 11323–11332, https://doi.org/10.1021/jacs.3c02399.

16. Z. Xing, L. Hu, D. S. Ripatti, X. Hu, and X. Feng, "Enhancing Carbon Dioxide Gas-Diffusion Electrolysis by Creating a Hydrophobic Catalyst Microenvironment," *Nature Communications* 12 (2021): 136, https://doi.org/10.1038/s41467-020-20397-5.

17. T. H. M. Pham, J. Zhang, M. Li, et al., "Enhanced Electrocatalytic CO_2 Reduction to C_{2+} Products by Adjusting the Local Reaction Environment With Polymer Binders," *Advanced Energy Materials* 12 (2022): 2103663, https://doi.org/10.1002/aenm.202103663.

18. Y. Lin, T. Wang, L. Zhang, et al., "Tunable CO_2 Electroreduction to Ethanol and Ethylene With Controllable Interfacial Wettability," *Nature Communications* 14 (2023): 3575, https://doi.org/10.1038/s41467-023-39351-2.

19. H. Yang, Q. Lin, C. Zhang, et al., "Carbon Dioxide Electroreduction on Single-Atom Nickel Decorated Carbon Membranes With Industry Compatible Current Densities," *Nature Communications* 11 (2020): 593, https://doi.org/10.1038/s41467-020-14402-0.

20. L. Jiao, J. Zhu, Y. Zhang, et al., "Non-Bonding Interaction of Neighboring Fe and Ni Single-Atom Pairs on MOF-Derived N-Doped Carbon for Enhanced CO_2 Electroreduction," *Journal of the American Chemical Society* 143 (2021): 19417–19424, https://doi.org/10.1021/jacs.1c08050.

21. L. Wang, H. Chen, Y. Wang, et al., "Recent Advances in Regulating the Local Environment of M-N_4 Structure for Tailored Chemical Reactions," *Nano Research* 16 (2023): 8596–8613, https://doi.org/10.1007/s12274-023-5510-8.

22. A. S. Varela, W. Ju, and P. Strasser, "Molecular Nitrogen–Carbon Catalysts, Solid Metal Organic Framework Catalysts, and Solid Metal/Nitrogen-Doped Carbon (MNC) Catalysts for the Electrochemical CO_2 Reduction," *Advanced Energy Materials* 8 (2018): 1703614, https://doi.org/10.1002/aenm.201703614.

23. B. Wang, M. Wang, Z. Fan, et al., "Nanocurvature-Induced Field Effects Enable Control Over the Activity of Single-Atom Electrocatalysts," *Nature Communications* 15 (2024): 1719, https://doi.org/10.1038/s41467-024-46175-1.

24. K. Li, Y. Kuwahara, and H. Yamashita, "Hollow Carbon-Based Materials for Electrocatalytic and Thermocatalytic CO_2 Conversion," *Chemical Science* 15 (2024): 854–878, https://doi.org/10.1039/D3SC05026B.

25. T. Chen, C. Fu, Y. Liu, et al., "Adsorption of Volatile Organic Compounds by Mesoporous Graphitized Carbon: Enhanced Organophilicity, Humidity Resistance, and Mass Transfer," *Separation and Purification Technology* 264 (2021): 118464, https://doi.org/10.1016/j.seppur.2021.118464.

26. Y. Rong, C. Pan, K. Song, et al., "Bamboo-Derived Hydrophobic Porous Graphitized Carbon for Adsorption of Volatile Organic Compounds," *Chemical Engineering Journal* 461 (2023): 141979, https://doi.org/10.1016/j.cej.2023.141979.

27. D. Guo, Y. Fu, F. Bu, et al., "Monodisperse Ultrahigh Nitrogen-Containing Mesoporous Carbon Nanospheres From Melamine-Formaldehyde Resin," *Small Methods* 5 (2021): 2001137, https://doi.org/10.1002/smtd.202001137.

28. Y. Ji, X. Liu, H. Li, X. Jiao, X. Yu, and Y. Zhang, "Hydrophobic ZIF-8 Covered Active Carbon for CO_2 Capture From Humid Gas," *Journal of Industrial and Engineering Chemistry* 121 (2023): 331–337, https://doi.org/10.1016/j.jiec.2023.01.036.

29. Z. Wang, Y. Xie, Y. Li, et al., "Tunable, Metal-Loaded Polydopamine Nanoparticles Analyzed by Magnetometry," *Chemistry of Materials* 29 (2017): 8195–8201, https://doi.org/10.1021/acs.chemmater.7b02262.

30. H. Zeng, D. S. Hwang, J. N. Israelachvili, and J. H. Waite, "Strong Reversible Fe^{3+} -Mediated Bridging Between Dopa-Containing Protein Films in Water," *Pnas* 107 (2010): 12850–12853, https://doi.org/10.1073/pnas.1007416107.

31. Y. Niu, X. Huang, X. Wu, L. Zhao, W. Hu, and C. Ming Li, "One-pot Synthesis of Co/N-Doped Mesoporous Graphene With Embedded Co/CoO_x Nanoparticles for Efficient Oxygen Reduction Reaction," *Nanoscale* 9 (2017): 10233–10239, https://doi.org/10.1039/C7NR03897F.

32. W. He, B. Tao, Z. Yang, et al., "Mussel-Inspired Polydopamine-Directed Crystal Growth of Core-Shell n-Al@PDA@CuO Metastable Intermixed Composites," *Chemical Engineering Journal* 369 (2019): 1093–1101, https://doi.org/10.1016/j.cej.2019.03.165.

33. B. Sun, Z. Li, D. Xiao, et al., "Unveiling pH-Dependent Adsorption Strength of $*CO^{-}$ Intermediate Over High-Density Sn Single Atom Catalyst for Acidic CO_2 -to-HCOOH Electroreduction," *Angewandte Chemie International Edition* 63 (2024): e202318874, https://doi.org/10.1002/anie.202318874.

34. W. Yang, H. Hu, Q. Pan, X. Deng, Y. Zhang, and Z. Shao, "Iron-Polydopamine Coated Multifunctional Nanoparticle SiO_2@PDA/Fe^{3+}-FA Mediated Low Temperature Photothermal for Chemodynamic Therapy of Cisplatin-Insensitive Osteosarcoma," *Materials & Design* 227 (2023): 111785, https://doi.org/10.1016/j.matdes.2023.111785.

35. Q. Li, Y. Jiao, Y. Tang, et al., "Shear Stress Triggers Ultrathin-Nanosheet Carbon Nitride Assembly for Photocatalytic H_2 O_2 Production Coupled With Selective Alcohol Oxidation," *Journal of the American Chemical Society* 145 (2023): 20837–20848, https://doi.org/10.1021/jacs.3c05234.

36. K.-J. Hsu, S. Li, M. Micari, et al., "Graphene Membranes With Pyridinic Nitrogen at Pore Edges for High-Performance CO_2 Capture," *Nature Energy* 9 (2024): 964–974, https://doi.org/10.1038/s41560-024-01556-0.

37. Z. Long, C. Yu, M. Cao, J. Ma, and L. Jiang, "Bioinspired Gas Manipulation for Regulating Multiphase Interactions in Electrochemistry," *Advanced Materials* 36 (2024): 2312179, https://doi.org/10.1002/adma.202312179.

38. Z. Zhao, L. Duan, Y. Zhao, et al., "Constructing Unique Mesoporous Carbon Superstructures via Monomicelle Interface Confined Assembly," *Journal of the American Chemical Society* 144 (2022): 11767–11777, https://doi.org/10.1021/jacs.2c03814.

39. R. Shi, J. Guo, X. Zhang, et al., "Efficient Wettability-Controlled Electroreduction of CO_2 to CO at Au/C Interfaces," *Nature Communications* 11 (2020): 3028, https://doi.org/10.1038/s41467-020-16847-9.

40. P. Wang, T. Hayashi, Q. Meng, et al., "Highly Boosted Oxygen Reduction Reaction Activity by Tuning the Underwater Wetting State of the Superhydrophobic Electrode," *Small* 13 (2017): 1601250, https://doi.org/10.1002/smll.201601250.

41. Y. Deng and B. S. Yeo, "Characterization of Electrocatalytic Water Splitting and CO_2 Reduction Reactions Using in Situ/Operando Raman Spectroscopy," *ACS Catal* 7 (2017): 7873–7889, https://doi.org/10.1021/acscatal.7b02561.

42. X. Chen, J. Chen, N. M. Alghoraibi, et al., "Electrochemical CO_2-to-Ethylene Conversion on Polyamine-Incorporated Cu Electrodes," *Nature Catalysis* 4 (2020): 20–27, https://doi.org/10.1038/s41929-020-00547-0.

43. Y. Cai, R. Yang, J. Fu, et al., "Self-Pressurizing Nanoscale Capsule Catalysts for CO_2 Electroreduction to Acetate or Propanol," *Nature Synthesis* 3 (2024): 891–902, https://doi.org/10.1038/s44160-024-00552-2.

44. J. Hao, Z. Zhuang, J. Hao, et al., "Strain Relaxation in Metal Alloy Catalysts Steers the Product Selectivity of Electrocatalytic CO_2 Reduction," *ACS Nano* 16 (2022): 3251–3263, https://doi.org/10.1021/acsnano.1c11145.

45. J. Wang, K. Zhang, T. T. T. Nga, et al., "Chalcogen Heteroatoms Doped Nickel-Nitrogen-Carbon Single-Atom Catalysts With Asymmetric Coordination for Efficient Electrochemical CO_2 Reduction," *Chinese Journal of Catalysis* 64 (2024): 54–65.

46. I. V. Chernyshova, P. Somasundaran, and S. Ponnurangam, "On the Origin of the Elusive First Intermediate of CO_2 Electroreduction," *Proceedings National Academy of Science USA* 115 (2018): E9261–E9270, https://doi.org/10.1073/pnas.1802256115.

47. X. Bai, C. Chen, X. Zhao, Y. Zhang, Y. Zheng, and Y. Jiao, "Accelerating the Reaction Kinetics of CO_2 Reduction to Multi-Carbon Products by Synergistic Effect Between Cation and Aprotic Solvent on Copper Electrodes," *Angewandte Chemie International Edition* 63 (2024): e202317512, https://doi.org/10.1002/anie.202317512.

Supporting Information

Additional supporting information can be found online in the Supporting Information section.

Supporting File: anie72852-sup-0001-SuppMat.docx.